compositional units but also delivered exogenous carbon-rich material to Vesta, a key ingredient for the formation and evolution of life on Earth.

References and Notes

1. H. Sierks *et al.*, *Space Sci. Rev.* **163**, 263 (2011).
2. K. Keil, in *Asteroid III*, William F. Bottke, Alberto Cellino, Paolo Paolicchi, Richard P. Binzel, Eds. (Univ. of Arizona Press, Tucson, 2002), pp. 573–584.
3. P. C. Thomas *et al.*, *Icarus* **128**, 88 (1997).
4. T. B. McCord, J. B. Adams, T. V. Johnson, *Science* **168**, 1445 (1970).
5. G. J. Consolmagno, M. J. Drake, *Geochim. Cosmochim. Acta* **41**, 1271 (1977).
6. J. Wisdom, *Nature* **315**, 731 (1985).
7. R. P. Binzel, S. Xu, *Science* **260**, 186 (1993).
8. Materials and methods are available as supplementary materials on *Science* Online.
9. M. J. Gaffey, *J. Geophys. Res.* **81**, 905 (1976).
10. L. Le Corre, V. Reddy, A. Nathues, E. A. Cloutis, *Icarus* **216**, 376 (2011).
11. J.-Y. Li *et al.*, *Icarus* **208**, 238 (2010).
12. M. C. De Sanctis *et al.*, *Science* **336**, 697 (2012).
13. D. W. Mittlefehldt *et al.*, *Planet. Mat.* **36**, 4-1 (1998).
14. P. Schenk *et al.*, *Science* **336**, 694 (2012).
15. A. Ruzicka, G. A. Snyder, *Meteor. Planet. Sci.* **32**, 825 (1997).

Coupling Quantum Tunneling with Cavity Photons

Peter Cristofolini,[1] Gabriel Christmann,[1] Simeon I. Tsintzos,[1,2] George Deligeorgis,[2]* George Konstantinidis,[2] Zacharias Hatzopoulos,[2] Pavlos G. Savvidis,[2,3] Jeremy J. Baumberg[1]†

Tunneling of electrons through a potential barrier is fundamental to chemical reactions, electronic transport in semiconductors and superconductors, magnetism, and devices such as terahertz oscillators. Whereas tunneling is typically controlled by electric fields, a completely different approach is to bind electrons into bosonic quasiparticles with a photonic component. Quasiparticles made of such light-matter microcavity polaritons have recently been demonstrated to Bose-condense into superfluids, whereas spatially separated Coulomb-bound electrons and holes possess strong dipole interactions. We use tunneling polaritons to connect these two realms, producing bosonic quasiparticles with static dipole moments. Our resulting three-state system yields dark polaritons analogous to those in atomic systems or optical waveguides, thereby offering new possibilities for electromagnetically induced transparency, room-temperature condensation, and adiabatic photon-to-electron transfer.

Strong coupling of photons to the interband exciton transition in a semiconductor microcavity leads to the formation of polaritons, bosonic quasiparticles whose properties are governed by their mixed light-matter composition. Owing to their quantum indistinguishability and the interplay of their Coulomb interactions, microcavity polaritons show unusually strong light-matter interactions and many-body quantum effects. In particular, their small effective mass allows observation of quantum degeneracy effects at temperatures from 10 to 300 K, such as Bose condensation (*1–4*) and superfluidity flow dynamics (*5*), and their tunable interactions make them ideal candidates for future quantum optoelectronic devices (*6*) working at room temperature (*7*). By contrast, spatially separating the electrons and holes in coupled double quantum wells yields indirect excitons with sufficiently long lifetimes for thermalization and a large static dipole moment (*8*). These properties enable efficient in-plane electrostatic traps (*9, 10*) and the coherent control of electron spins (*11*). By embedding double quantum wells inside a conventional microcavity in the strong coupling regime, we unite the concepts of indirect excitons and microcavity polaritons to produce optically active quasiparticles with transport properties, named dipolaritons. These offer the advantages of both systems: electrical trapping and tuning of excitons, strong optical coupling to low-mass quasiparticles with large de Broglie wavelength, and excellent control over the dipole properties and interactions (*12, 13*).

Microcavities are formed from p-i-n semiconductor multilayers surrounded by doped multilayer mirrors (*7*) (Fig. 1A; details in the supporting online material) and pumped with a nonresonant laser. Quantum wells (QWs) of InGaAs inside the cavity are arranged in asymmetric pairs separated by a thin barrier (of width L_B) that allows electrons to tunnel between the two wells (Fig. 1A). Because of the large effective hole mass and the wide energy separation of hole levels in neighboring QWs, hole tunneling is negligible, and only the low-energy left QW (LQW) hole state is considered. Without tunneling, there are two types of exciton in this system. The direct exciton $|DX\rangle$ has both electron and hole in the left QW (Fig. 1B, top) and therefore strongly couples to the cavity mode, with its induced dipole moment oriented randomly in the QW plane. The indirect exciton $|IX\rangle$ has the hole in the left QW and the electron in the right QW—thus possessing an additional static dipole moment aligned perpendicularly to the plane—and has a very small overlap of electron and hole wave functions, hence low oscillator strength. When a bias voltage is applied to bring the electron levels into resonance, the electron states in the two QWs mix to give symmetric and antisymmetric electron wave functions (red in Fig. 1A), which, together with the low-energy hole states (blue) in the left QW, produce the exciton modes $(1/\sqrt{2})\{|IX\rangle \pm |DX\rangle\}$, split by the tunneling energy $\hbar J$ (where $\hbar$ is Planck's constant divided by 2π). These modes combine the large oscillator strength of the DX with the large static dipole moment of the IX (Fig. 1B, bottom).

Embedding DX and IX excitons in the microcavity with cavity mode C now forms a three-state system similar to the atomic Λ-scheme (*14, 15*), which is coupled optically by the vacuum Rabi frequency Ω and electronically by the electron tunneling rate J (Fig. 1C). Although J and Ω are intrinsic to the microcavity design, full control of the dipolariton modes is possible through bias voltage control of tunneling and angle tuning of the cavity mode. In the strong coupling regime, when J is larger than the carrier escape rate from the coupled QWs and Ω is faster than the photon decay rate, the system displays three distinct eigenmodes: the lower (LP), middle (MP), and upper (UP) dipolaritons. Thus, a conventional microcavity polariton (Fig. 1D, black) can be simply bias-tuned to yield the dipolariton spectrum (red) in the strong tunneling regime.

The bias dependence of the photoluminescence (PL) of a mesa with barrier width $L_B = 4$ nm (Fig. 2) clearly reveals these three dipolariton modes. Because in-plane wave vectors k are conserved, photons emitted at an angle θ directly measure dipolaritons at k. At normal incidence (Fig. 2, A and C) the narrow cavity mode is detuned below the excitons, whereas at 35° (Fig. 2, B and D) the uncoupled modes are all degenerate. For higher electric fields, the PL emission weakens because electrons escape the coupled QW system before they can recombine radiatively with a left QW hole, and eventually two of the modes vanish, leaving only the most cavity-

[1]NanoPhotonics Centre, Cavendish Laboratory, University of Cambridge, Cambridge CB3 0HE, UK. [2]FORTH-IESL, Post Office Box 1527, 71110 Heraklion, Crete, Greece. [3]Department of Materials Science and Technology, University of Crete, Post Office Box 2208, 71003 Heraklion, Greece.

*Present address: CNRS, LAAS, 7 avenue de Colonel Roche, F-31077 Toulouse Cedex 4, France.
†To whom correspondence should be addressed. E-mail: jjb12@cam.ac.uk

Fig. 1. (A) Schematic band structure of coupled quantum wells in a microcavity at tunneling resonance. As a result of tunneling coupling J, electrons (red wave functions) extend over both wells while holes (blue) are confined in the LQW. Strong optical coupling to cavity photons Ω gives rise to dipolaritons. DBR, distributed Bragg reflector. **(B)** Conventional in-plane excitons (top) acquire a static out-of-plane dipole moment at resonance (bottom). **(C)** Three-level Λ-scheme coupling cavity C and direct (DX) and indirect (IX) exciton modes by classical intense laser pump Ω and quantum tunneling J. **(D)** Spectra of standard polaritons (black) and dipolaritons (red) tuned with bias.
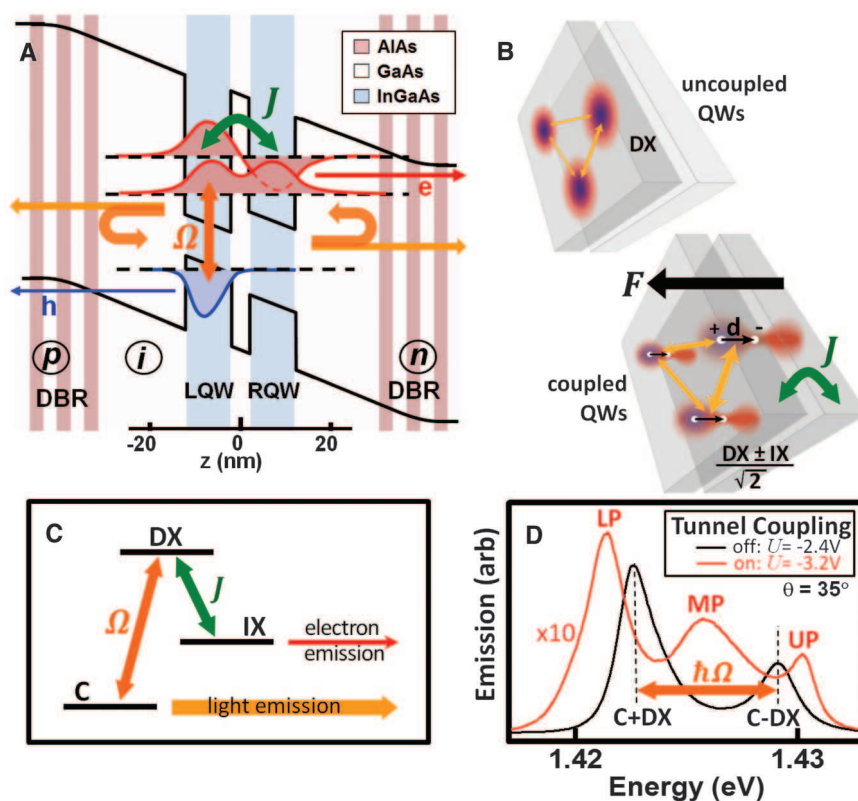
like dipolariton. A simple harmonic oscillator model coupling the modes $\{|IX\rangle, |DX\rangle, |C\rangle\}$ gives a deeper understanding of these dipolaritons. The Hamiltonian H is

$$H = \hbar \begin{pmatrix} \omega_{IX} & -J/2 & 0 \\ -J/2 & \omega_{DX} & -\Omega/2 \\ 0 & -\Omega/2 & \omega_C \end{pmatrix} \quad (1)$$

where $|DX\rangle$ couples to both $|IX\rangle$ and $|C\rangle$, whereas there is no direct interaction between $|IX\rangle$ and $|C\rangle$ (Fig. 1C) (16). Independent control over all parameters in this model is practical: Angle tuning shifts the cavity frequency, bias voltage tunes both the IX level (directly) and the DX level (as a result of the quantum confined Stark effect), the barrier width sets the intrinsic tunneling rate J, and Ω is set by the microcavity design and geometry. Diagonalization of H yields the three dipolariton modes $|LP\rangle$, $|MP\rangle$, and $|UP\rangle$, which provide an excellent account of the PL (Fig. 2, A and B, and Fig. 3A, solid lines, with uncoupled modes dashed).

At normal incidence (Fig. 2, A and C), the cavity mode is detuned 10 meV below the excitons and hence is effectively decoupled from the excitons. The weak exciton PL nonetheless directly resolves their tunnel splitting $\hbar J$ at the anticrossing bias $U = -3.2$ V (Fig. 3D, black curve). This situation changes at high angle (Fig. 2, B and D), where the cavity mode is resonant with both the direct and indirect exciton transition. For low bias voltage, IX is far detuned and
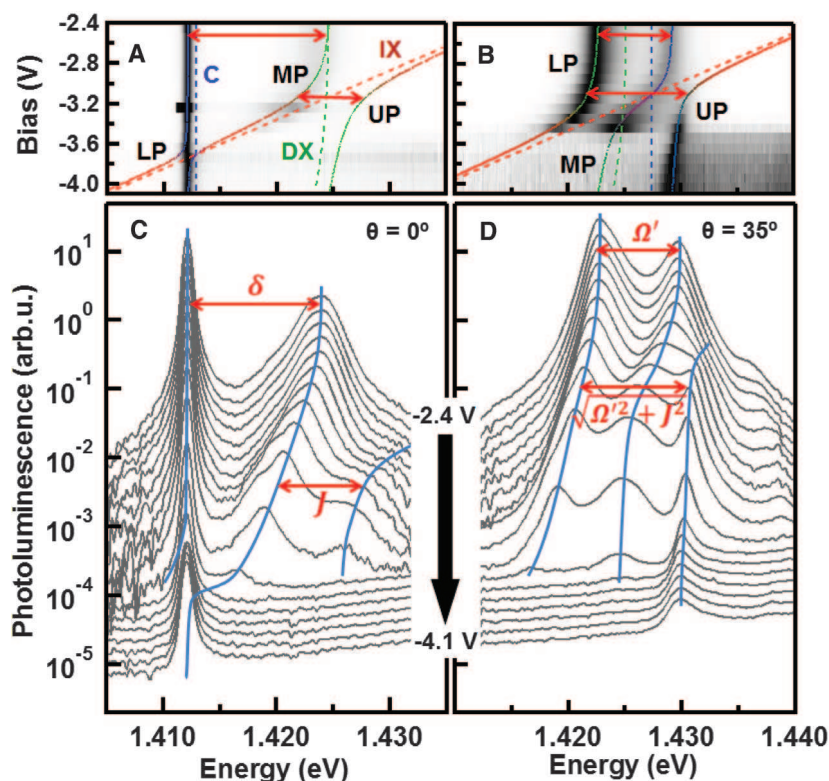
Fig. 2. (A to D) Normalized PL spectra with bias voltage for the off-resonant cavity [(A) and (C)] and close to resonance [(B) and (D)] for a mesa with $L_B = 4$ nm. Polariton lines LP, MP, and UP in (A) and (B) are fits to the coupled oscillator model of Eq. 1; dashed lines show the uncoupled modes: cavity (C, blue), direct (DX, green), and indirect (IX, red) excitons. In (C) and (D) the spectra are shifted for clarity; blue lines are guides to the eye.

the system behaves as a single-QW microcavity with direct excitons only, producing detuned Rabi splitting $\Omega' = \sqrt{\Omega^2 + \delta^2}$, where $\delta(U, \theta)$ is the detuning of DX below C at each bias and angle. Simultaneous resonance of DX, IX, and the cavity mode is reached again at $U = -3.2$ V and appears as three clearly distinct dipolariton branches spanned by an anticrossing of width $S = \sqrt{\Omega'^2 + J^2}$. The eigenvectors at resonance (when $\omega_C = \omega_{IX} = \omega_{DX} + \delta$) are

$$|MP\rangle = \alpha\{\Omega|IX\rangle - J|C\rangle\} \qquad (2)$$

$$\begin{vmatrix} UP \\ LP \end{vmatrix} = \beta\{J|IX\rangle + \Omega|C\rangle - (\delta \pm S)|DX\rangle\} \quad (3)$$

Remarkably, although the central MP has no DX admixture at resonance (independent of the detuning δ), it is clearly visible in emission through the tunneling interaction with the cavity photon (and is almost as strong as the other dipolaritons). The absence of DX in the MP arises from the destructive interference of transition amplitudes, as seen in Fig. 3B, which shows the composition of each of the dipolariton modes versus bias, extracted from the coupled oscillator model of Fig. 3A. With increasing field, the MP turns from an ordinary DX polariton to a pure dipolariton at resonance (black arrow), consisting only of $|IX\rangle$ and $|C\rangle$ (Eq. 2), with the electron and hole located in different QWs and possessing a static dipole moment oriented perpendicularly to the QW plane (Fig. 1B).

In atomic physics, this state is known as a dark polariton (14, 15) and is used for electromagnetically induced transparency (EIT) (17) in atomic media or waveguides (18), for drastic slowing of light propagation (19), and for light storage (20, 21). The MP dipolariton differs from atomic dark polaritons in that the role of the second probe laser in the Λ-scheme is now taken by the bias-controlled electron tunneling transition. Applying EIT to a condensed dipolariton population could thus map photonic states onto electron tunneling states that can be read out in charge transport. This suggests new strategies for quantum readout and optical interconnects—for example, as a variable pulse delay element in dipolariton signal processing. Furthermore, interactions between dipolaritons with vertically aligned dipole moments are much stronger (by a factor of 100) than for typical dipole-dipole scattering between in-plane excitons (22) and resemble an ensemble of Rydberg atoms in an electric field (23). The stronger repulsion of dipolaritons over conventional polaritons leads to increased stimulated scattering rates, and hence lower condensation thresholds (22). We suggest that this is a fruitful approach to accessing room-temperature polariton condensates.

The bare tunneling rate J controls the coupling between the two exciton modes and is set by the width and height of the barrier between the QWs. To test the tunnel control of dipolaritons, we fabricated devices with barrier widths of 4 nm, 7 nm, and 20 nm. Emission PL

measurements (Fig. 3A and fig. S2) confirm the dependence of strong coupling dipolariton modes on this tunneling rate. Extracting the polariton Rabi splittings from each sample gives $\hbar\Omega = 6.0$ meV, whereas the tunnel splitting varies from $\hbar J = 0$ to 6 meV (Fig. 3A, inset), which proves that small tunneling barriers L_B are required to see dipolaritons. The tunnel splitting J exactly matches (Fig. 3A, line in inset) that from parameter-free solutions of the Schrödinger equation for this asymmetric double QW with electric field (13), showing the expected exponential decrease in splitting with increased barrier width. The excellent fits confirm the simple explanatory power of this model for the observed modes.

Resonant dipolariton systems offer new ways to control tunneling. When Rabi flopping is faster than tunneling ($J < \Omega$), the dipolariton spends half of the time rapidly oscillating between a cavity photon and a DX (Fig. 3C). Because the excitation is not available for tunneling when it is a cavity photon, this results in a reduced effective tunneling rate $J_{eff} = J/\sqrt{2}$. On the other hand, in the fast tunneling limit $J > \Omega$, the electron is only in the left QW for half the time, which reduces the coupling to the cavity photon and hence

reduces the effective Rabi splitting. Thus, modifying the admixture of C and DX in the MP allows optical control of the tunneling process: Optical and electrical detunings determine the amount of time the electron spends shuttling between the left and right QWs or Rabi flopping on the DX transition. The anticrossings in the energy dispersion of LP-MP and MP-UP (figs. S4 and S5) quantify this effective tunneling rate J_{eff}, depending on J, Ω, and detunings between the modes.

Such polariton mesas can be sensitively switched (fig. S3), toggling between the regimes of conventional polaritons and of strongly tunnel-coupled dipolaritons with a small change in bias voltage U (Fig. 1D) or in cavity angle θ (Fig. 3D). Furthermore, electrical manipulation of the coupling of the dipolariton static dipole moment to light is possible (fig. S4D).

The observation and control of dipolaritons in these electrical devices opens up interesting regimes for quantum optoelectronics, combining quantum tunneling with light-matter coupling. The full control of the modes in this system (with bias voltage tuning and angle tuning), together with the enhancement of dipolariton repulsion relative to conventional microcavity polaritons,
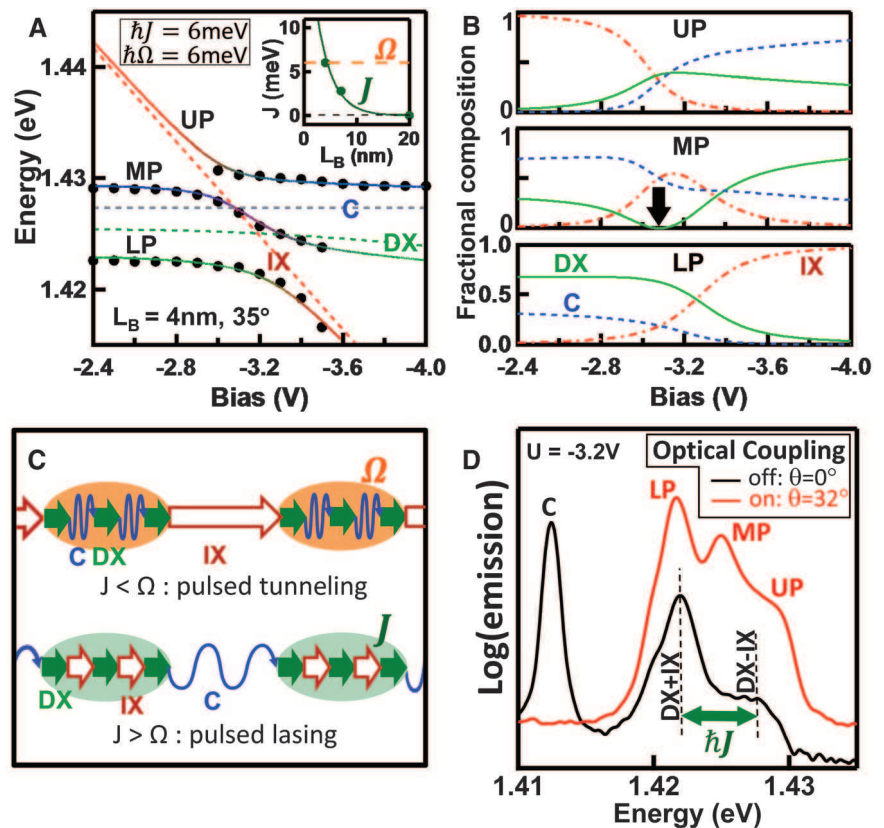
Fig. 3. (**A**) Bias-dependent polariton modes observed in photoluminescence for $L_B = 4$ nm with fits to the coupled oscillator model of Eq. 1. Inset: Extracted intrinsic tunneling rate J as a function of the barrier width (points) together with theory (line). (**B**) Bias dependence of the polariton composition; black arrow for MP marks position of the pure dipolariton of Eq. 2. (**C**) For $J < \Omega$, tunneling is suppressed; for $J > \Omega$, the Rabi frequency is reduced. (**D**) Optical control of the dipolariton regime by changing from red-detuned cavity (black) to resonance (red) through angle tuning.

implies that they are strong candidates for high-temperature condensates with tunable interactions. The pure dipolariton EIT state, consisting only of cavity and indirect exciton components, offers a Λ transition scheme amenable to building coherence between light and matter states, and thereby directly applicable to novel adiabatic photon-to-electron transfer.

References and Notes

1. J. Kasprzak *et al.*, *Nature* **443**, 409 (2006).
2. S. Christopoulos *et al.*, *Phys. Rev. Lett.* **98**, 126405 (2007).
3. R. Balili, V. Hartwell, D. Snoke, L. Pfeiffer, K. West, *Science* **316**, 1007 (2007).
4. K. G. Lagoudakis, B. Pietka, M. Wouters, R. André, B. Deveaud-Plédran, *Phys. Rev. Lett.* **105**, 120403 (2010).
5. A. Amo *et al.*, *Nature* **457**, 291 (2009).
6. F. Capasso, *Science* **235**, 172 (1987).
7. S. I. Tsintzos, N. T. Pelekanos, G. Konstantinidis, Z. Hatzopoulos, P. G. Savvidis, *Nature* **453**, 372 (2008).
8. Z. Vörös, D. W. Snoke, L. Pfeiffer, K. West, *Phys. Rev. Lett.* **103**, 016403 (2009).
9. A. A. High, E. E. Novitskaya, L. V. Butov, M. Hanson, A. C. Gossard, *Science* **321**, 229 (2008).
10. G. Schinner *et al.*, *Phys. Rev. B* **83**, 165308 (2011).
11. M. Poggio *et al.*, *Phys. Rev. B* **70**, 121305 (2004).
12. G. Christmann *et al.*, *Phys. Rev. B* **82**, 113308 (2010).
13. G. Christmann *et al.*, *Appl. Phys. Lett.* **98**, 081111 (2011).
14. M. Fleischhauer, M. D. Lukin, *Phys. Rev. Lett.* **84**, 5094 (2000).
15. M. D. Lukin, S. F. Yelin, M. Fleischhauer, *Phys. Rev. Lett.* **84**, 4232 (2000).
16. The minimal splitting between LP and MP in Fig. 2A illustrates the absence of direct coupling between IX and C, justifying $H_{13} = H_{31} = 0$ in Eq. 1.
17. M. Mücke *et al.*, *Nature* **465**, 755 (2010).
18. M. F. Yanik, W. Suh, Z. Wang, S. Fan, *Phys. Rev. Lett.* **93**, 233903 (2004).
19. M. D. Lukin, A. Imamoğlu, *Nature* **413**, 273 (2001).
20. D. F. Phillips, A. Fleischhauer, A. Mair, R. L. Walsworth, M. D. Lukin, *Phys. Rev. Lett.* **86**, 783 (2001).
21. C. Liu, Z. Dutton, C. H. Behroozi, L. V. Hau, *Nature* **409**, 490 (2001).
22. A. Filinov, N. V. Prokof'ev, M. Bonitz, *Phys. Rev. Lett.* **105**, 070401 (2010).
23. D. Møller, L. B. Madsen, K. Mølmer, *Phys. Rev. Lett.* **100**, 170504 (2008).

Under the Hood of the Earthquake Machine: Toward Predictive Modeling of the Seismic Cycle

Sylvain Barbot,[1]* Nadia Lapusta,[1,2] Jean-Philippe Avouac[1]

Advances in observational, laboratory, and modeling techniques open the way to the development of physical models of the seismic cycle with potentially predictive power. To explore that possibility, we developed an integrative and fully dynamic model of the Parkfield segment of the San Andreas Fault. The model succeeds in reproducing a realistic earthquake sequence of irregular moment magnitude (M_w) 6.0 main shocks—including events similar to the ones in 1966 and 2004—and provides an excellent match for the detailed interseismic, coseismic, and postseismic observations collected along this fault during the most recent earthquake cycle. Such calibrated physical models provide new ways to assess seismic hazards and forecast seismicity response to perturbations of natural or anthropogenic origins.

S eismic and geodetic observations provide an increasingly detailed insight into fault motion over a wide range of temporal and spatial scales, from rapid seismic rupture to slower postseismic slip and complex interseismic behavior, including slow episodes of accelerating slip and tremor (*1–5*). Laboratory experiments and theoretical developments (*6–13*) provide an increasingly detailed physical basis for understanding the entire earthquake cycle. Yet, models capable of capturing a wide range of observations are still in their infancy. Existing models are either restricted to specific aspects of fault behavior (e.g., progression of a single dynamic rupture or evolution of postseismic slip) or simplify some stages of the fault deformation (*14–20*). Recently developed numerical methods (*21–23*) allow us to resolve, in one physical model, slow tectonic loading, earthquake nucleation, and

rupture propagation—including the radiation of seismic waves—and the afterslip transient that follows main shocks, but so far these methods have been applied to qualitative studies of conceptual fault scenarios (*24*).

We have developed a fully dynamic model of the earthquake cycle capable of quantitatively reproducing a wide range of observations for the Parkfield segment of the San Andreas Fault (SAF) (Fig. 1). The Parkfield sequence of moment magnitude (M_w) 6.0 events, their inferred similarities, and their short recurrence times inspired one of the most famous prediction experiments and prompted the installation of modern seismic and geodetic networks (*25, 26*). The latest rupture of 2004 defied the expectations by taking place a decade later than anticipated and initiating on the opposite end of the segment compared with previous events (*27*). Interestingly, a series of smaller earthquakes occurred in 1993 around the location where the 1966 event had nucleated (Fig. 1), but they failed to generate the M_w 6.0 event that was expected at the time (*1*). Due to the dense instrumentation networks and other observational facilities, such as the San Andreas Fault Observatory at Depth

(*13*), installed to monitor the Parkfield segment, the pattern of strain buildup, microseismic activity in the interseismic period, as well as co- and postseismic deformation related to the 2004 earthquake cycle, have been relatively well constrained (*27–31*).

Our dynamic model of the earthquake cycles at Parkfield is constrained by multiple sets of observations and previous theoretical findings. We use the spatial pattern of microseismicity, the time series of Global Positioning System (GPS) displacements in the 1999 to 2010 period, the interferometric synthetic aperture radar (InSAR) data, and the GPS offsets of the 2004 earthquake (*2, 4, 19, 29, 32*). We also consider the slip distribution of the 1966 event and the historical catalog of recurrence times and hypocenter locations of M_w 6.0 events (*25*). As an integration device for all observations, we adopt a strike-slip fault segment embedded into an elastic medium, loaded by a deep-seated slip at the long-term slip rate, and governed by rate-and-state friction, a well-established empirical constitutive law for fault strength (*6–8, 10*). The area with rate-weakening friction, where seismic slip can nucleate, is bounded to the north and south by rate-strengthening patches. The northern rate-strengthening patch accounts for the creeping segment of the SAF. The southern one is more speculative; it serves as a possible proxy for the kind of barrier effect needed to account for the repetition of similar events arresting in that area and for an as-yet-unknown source of localized stressing (*35*).

The model results in a rich history of fault slip with spontaneous nucleation and ruptures of earthquakes of magnitudes ranging from M_w 2.0 to 6.0 (Fig. 2 and movie S1). The simulated M_w 6.0 earthquake cycles reproduce co-, post-, and interseismic behavior of the Parkfield segment, with most coseismic slip occurring in the area circumscribed by microseismicity. The simulated sequence of earthquakes includes the nucleation of a rupture near the hypocenter of the

[1]Division of Geological and Planetary Sciences, California Institute of Technology, 1200 East California Boulevard, Pasadena, CA 91125, USA. [2]Division of Engineering and Applied Sciences, California Institute of Technology, 1200 East California Boulevard, Pasadena, CA 91125, USA.

*To whom correspondence should be addressed. E-mail: sbarbot@caltech.edu